International Journal of Applied Science and Engineering

Determination of the defect's size of multi-layer woven CFRP based on its temperature profile

Muhamad Hidayat[1], Chih-Hung Chiang[2, 3*], Max Yen[2]

[1] *Department of Construction Engineering, Chaoyang University of Technology, 168, Jifeng E. Rd., Wufeng District, Taichung City 413310, Taiwan*
[2] *Department of Aeronautical Engineering, Chaoyang University of Technology, 168, Jifeng E. Rd., Wufeng District, Taichung City 413310, Taiwan*
[3] *Center for NDT, Chaoyang University of Technology, 168, Jifeng E. Rd., Wufeng District, Taichung City 413310, Taiwan*

ABSTRACT

Physical phenomena in thin multi-layer carbon fiber reinforced polymer (CFRP) materials with defects are not always easily definable through experimental observations of thermography nondestructive testing (TNDT). The current research focuses on the transient heat distribution of the finite element model of a seven-layer CFRP plate with embedded defects. The simulated heating load is applied at the back surface of the three-dimensional FE model such that the thermal analysis is carried out to characterize the temperature profiles along various observation lines across the front surface. The sizes of the embedded defects at different depths are estimated by the full width half maximum (FWHM) method. The simulation results are verified experimentally against a CFRP specimen based on the same model design using active thermography. The defect sizes can be determined successfully by FWHM only if the surface temperature profiles are pre-processed by the data averaging technique.

Keywords: CFRP materials, TNDT, Finite element method, Simulation, Defect size.

OPEN ACCESS

Received: February 7, 2023
Revised: March 31, 2023
Accepted: April 10, 2023

Corresponding Author:
Chih-Hung Chiang
chiangc@cyut.edu.tw

Copyright: The Author(s). This is an open access article distributed under the terms of the Creative Commons Attribution License (CC BY 4.0), which permits unrestricted distribution provided the original author and source are cited.

Publisher:
Chaoyang University of Technology
ISSN: 1727-2394 (Print)
ISSN: 1727-7841 (Online)

1. INTRODUCTION

Thermography nondestructive testing (TNDT) is based on measuring the distribution of surface temperatures to determine the shape (Sirikham et al., 2020), size (Vavilov, 2022; Zhou et al., 2023), and depth (Wang et al., 2022) of underlying defects. This test may involve an experiment or a theoretical solution. Experiments using TNDT have been frequently utilized to assess the damage to composite structures (Poelman et al., 2020; Xu et al., 2020; Marani et al., 2023). However, this technology is typically time-consuming and expensive (Vavilov and Burleigh, 2020).

Defects may occur during the fabrication of composites and their in-service life. Some types of defects are resin cracks or transversal ply cracks, voids, porosity, and debonded interlaminar regions (Meola et al., 2016). In recent years, theoretical research utilizing numerical analysis to detect defects has been conducted with computers' incredibly rapid data processing capabilities (Zalameda and Winfree, 2018; Quintanas-Corominas et al., 2019). Experimental case analysis and TNDT boundary determination will be done efficiently using numerical modelling (Vavilov, 2022). In addition, this simulation method helps to simplify the experimental design (Chiang and Hidayat, 2022).

This study explores the results obtained from the TNDT simulation using the finite element method to better characterize defects contained in CFRP materials which is not easy to do through TNDT experiments. This research approach is based on the work by Vavilov (2022), with the distinction in the kind of materials, the form, and the conditions of the defects. The experiment was conducted to verify the simulation result using the test specimen with size, material, and layering of the carbon fiber as close as

the simulation model. Some treatments were also made to the experimental setup to reduce the environmental effect. As a continuation of the previous research by Chiang and Hidayat (2022), this study focuses on identifying the detected defect's size and accuracy compared to its real size.

This paper begins with a simulation aspect that describes the constructed model, finite element modelling, and the applied equations. The following section explains the experiment consisting of the test specimen properties, experimental setup, and how the experiment is carried out. Furthermore, the simulation and experiment results are presented in graphs and tables subsequently discussed. Some conclusions are drawn in the end.

2. SIMULATION

Ansys® software environment was utilized for the simulation. The model is prepared in Ansys SpaceClaim and Ansys Composite PrePost (ACP), and then the model is processed using Ansys Mechanical's analysis tools to determine the surface temperature profile. The data from simulation software is subsequently processed in spreadsheet software.

2.1 The Model

The model is a woven rectangular CFRP prepreg, stacked into seven layers with the stacking sequence being [+45/0/-45/0/-45/0/+45]. The front and back surfaces are flat, with a thickness of 1.96 mm. The model dimension is shown in Fig. 1, and all dimensions are in mm.

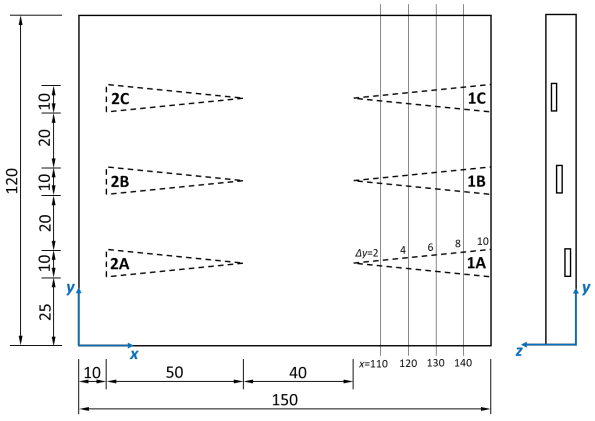

Fig. 1. Model dimension

The types of defects analyzed are only void defects (1A, 1B, 1C), not inserted material defects (2A, 2B, 2C), due to the difficulty in detecting the differences in the defects' surface heat distribution and its surroundings (Chiang and Hidayat, 2022). The void defects represent the inter-laminar debonding of the ply inside the composite is filled by air. All defects are isosceles triangular with the size of 10 mm × 50 mm. The defect width will decrease as its placement along the triangle height increases. The defect width will be measured at positions x = 150, 140, 130, 120 and 110 mm, which correspond to the defect width, Δy, being 10, 8, 6, 4 and 2 mm, respectively. Defects and materials properties are shown in Table 1 and Table 2. The depths of the defects are measured from the front surface.

Table 1. Defects property

Defect	Thickness (mm)	Depth (mm)
1A/2A	0.28	1.40
1B/2B	0.28	0.84
1C/2C	0.28	0.28

Table 2. Material property

Material	Thermal conductivity (W/m.K)			Specific heat (J/kg.K)	Thickness (mm)
	X	Y	Z		
Woven CFRP prepreg	3.1	3.1	0.6	1000	0.28
Air (void)		0.026		1021	0.28

2.2 Finite Element Modeling

The software determines the type of elements utilized in developing the mesh model, solid278 and surf152, except for the 0.25 mm mesh size selection. The heat loading was evenly subjected to the model's back surface, with the magnitude seen in Fig. 2.

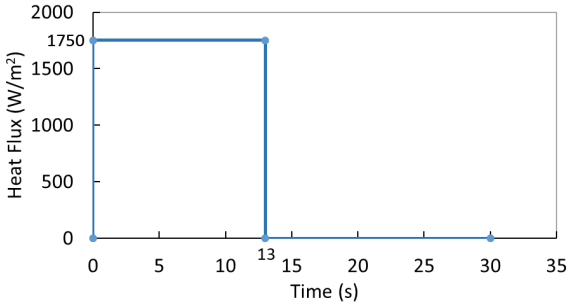

Fig. 2. Heat loading

The model is let to cool down naturally with the heat convection occurring at the front surface at the rate of 2.5 /Wm^{2}K and the back and sides surfaces at the rate of 1.0 /Wm^{2}K. The ambient temperature was set to 27°C, the same as the experiments.

3. EXPERIMENT

3.1 Test Specimen

The test specimen's dimensions, materials, and fiber layers are like the simulation's model. A dry lay-up by hand was used to make the test specimen. The void defects were made by putting thin steel inserts in a cut CFRP sheet and then removed after the curing process. The test specimen was manufactured using a mold under a pressure of 1.0 MPa and cured at 150°C. The finished test specimen looks like in

Fig. 3, with white dashed lines representing the void defects' position. During the preparation of test specimens, care must be taken to avoid failure mechanisms that can occur in the machining of CFRP (Karataş, 2018).

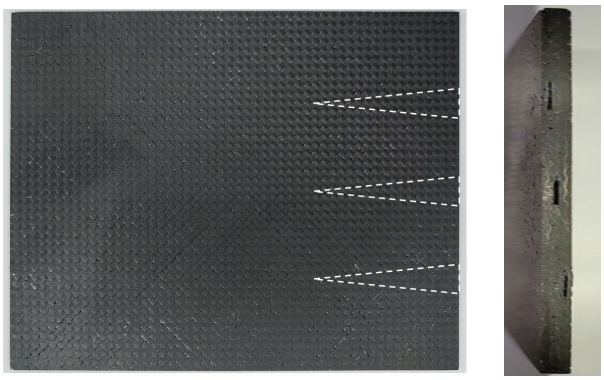

(a) (b)

Fig. 3. (a) Specimen front surface and (b) the void defects

3.2 Experimental Setup

The specimen is placed between the camera and the lamp in the experiment. The lamp will emit infrared light on the specimen's back surface, and the camera will record a thermal image on the specimen's front surface. The equipment specification is given in Table 3, and the experimental layout is shown in Fig. 4.

Table 3. Equipment specification

Equipment	Specification
Camera	
Type	Infrared
Name	AVIO InfReC R500EX
Resolution (pixel)	640 × 480 (standard)
Measuring range (°C)	1280 × 960 (Super resolution)
Sensitivity (°C)	-40 to 120 or 0 to 500
Heat source	
Type	General infrared lamp
Power (W)	175

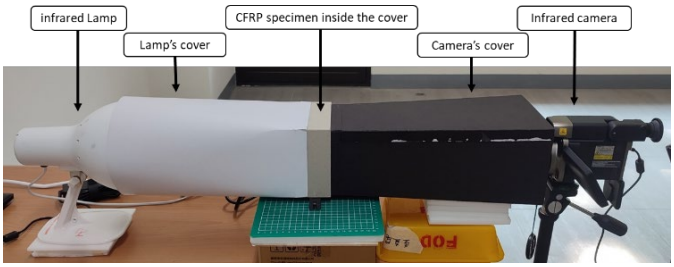

Fig. 4. Experimental layout

The camera cover reduces heat distortion reading from the environment, and the lamp cover provides direct infrared light so that it is more focused and evenly distributed to the back surface of the specimen. Specimen cover helps to isolate the specimen from environmental influences.

3.3 Thermography Data

Construction lines are sketched to pick the temperature data at x = 110 mm (a), x = 120 mm (b), x = 130 mm (c), x = 140 mm (d), and x = 150 mm (e), as seen in Fig. 5.

The specimen shape in the temperature image is not precisely rectangular as in the real one. It is caused by camera lens distortion. The specimen's boundaries are not precisely identified due to the heat distribution in those areas. The start and finish points of the construction lines and the line at x = 150 mm are not their exact positions but are the closest points that can be determined.

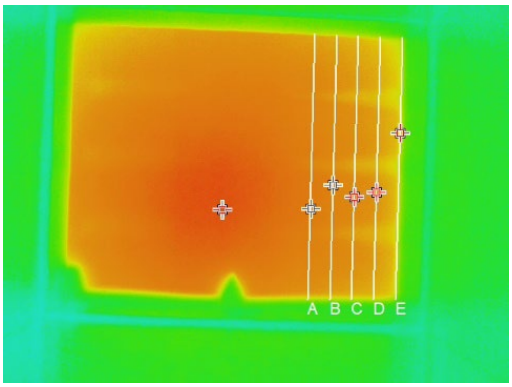

Fig. 5. The construction line in the thermography image

4. FULL WIDTH HALF MAXIMUM AND TEMPERATURE PROFILE DERIVATIVE

Full width half maximum (FWHM) measures the distance between points corresponding to half of the maximum temperature signal, $\Delta T_m/2$ (Avdelidis, 2004). The extrema of $T(x, y)$ derivatives along every surface direction precisely match the defect boundary projections onto any sample surface (Vavilov and Burleigh, 2020). T_m is the maximum temperature profile value.

The temperature distribution over specimen surfaces for the observed time will be generated in simulation and experiment. The defect size can be determined from its temperature profile first derivative, $\delta T/\delta y$.

The temperature profile data is discrete, and so is its derivative. The first derivative is calculated using the equations:

$$\frac{dT}{dy} = \frac{T_{i+1} - T_1}{y_{i+1} - y_i} \quad (1)$$

Where T and y are the temperature and position of a node along the y-axis.

The accuracy of the temperature profile and its derivative can be enhanced by refining the model's finite element meshing in simulation and increasing the camera's resolution in the experiment.

5. RESULTS AND DISCUSSION

5.1 Simulation Results

Fig. 6 shows the simulation temperature profiles and their first derivative for every x position and time, t, reviewed. The temperature values are almost constant on the no-defect area's x- and y-axis. It happens because the heat flux is applied evenly on the specimen's back surface. It is shown that even after the heat flux was removed (at t = 13 s), the front surface temperature rises until a certain time.

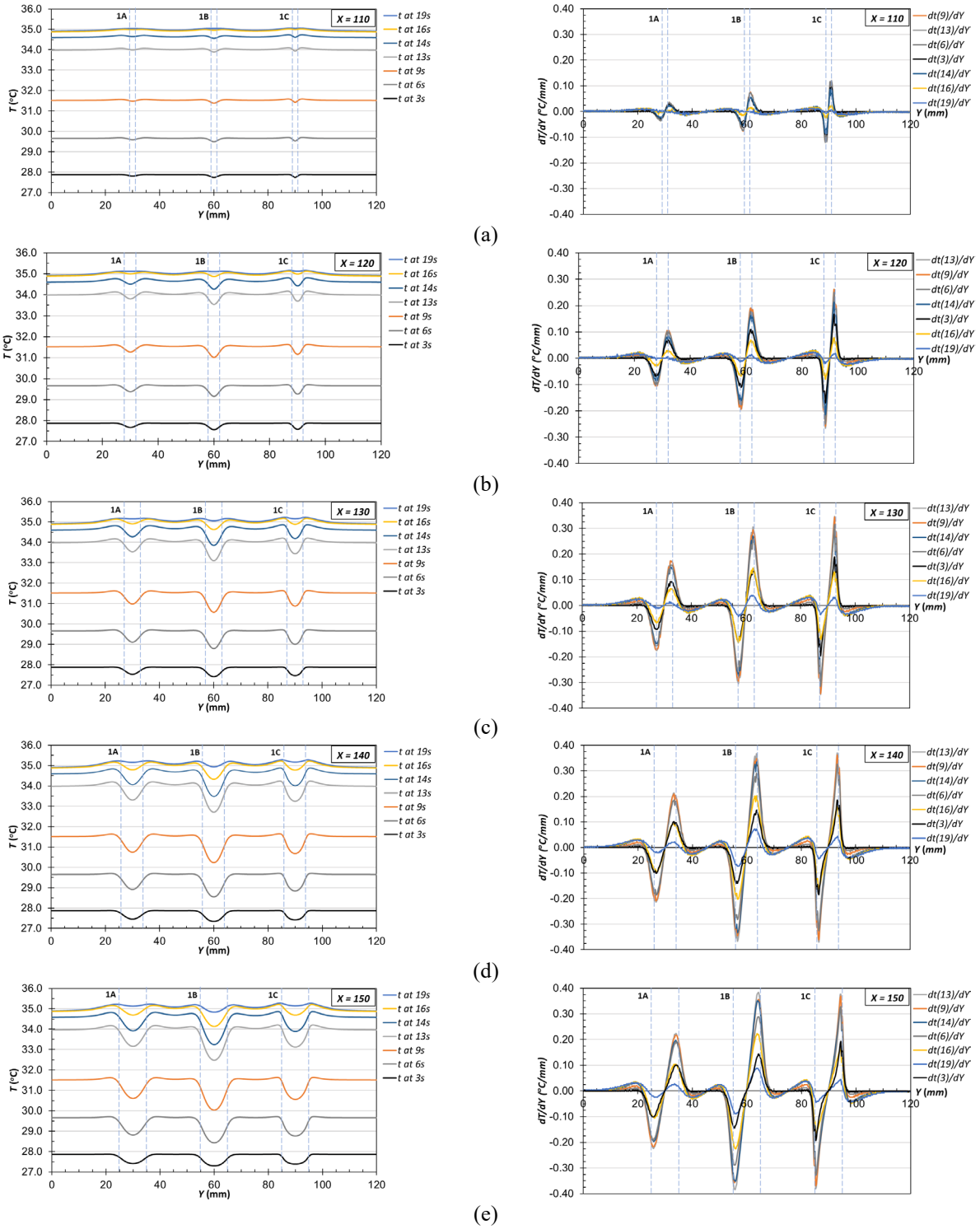

Fig. 6. Simulation temperature profiles and their first derivative: (a) x = 110, (b) x = 110, (c) x = 130, (d) x = 140, and (e) x = 150

The simulation temperature profile shows the defect position clearly and precisely at every x most of the time, except at t = 19 s for x = 110 and x = 120. The bigger the defect width, the higher its first derivative value. The shallower the defect, the easier it is to be detected. In this case, the most detectable defect is 1C, followed by 1B and 1A.

Table 4 shows the defects' width and accuracy simulation results compared to the defects' real width based on the first derivative curve.

Table 4. Simulation defects' width

x-axis	Defects	1A		1B		1C	
		Width	Δ	Width	Δ	Width	Δ
	Real width			2.0			
	t = 3 s	3.2	59%	2.2	10%	2.2	10%
	t = 6 s	3.2	59%	2.2	10%	2.2	10%
	t = 9 s	3.2	59%	2.7	34%	2.2	10%
x = 110	t = 13 s	3.2	59%	2.2	10%	2.2	10%
	t = 14 s	2.7	34%	3.2	59%	2.2	10%
	t = 16 s	4.9	147%	2.7	34%	2.2	10%
	t = 19 s	6.7	236%	6.0	199%	1.9	-3%
	Average (abs)	3.9	93%	3.0	51%	2.2	10%
	Real width			4.0			
	t = 3 s	3.1	-22%	3.1	-22%	3.1	-22%
	t = 6 s	3.6	-9%	3.1	-22%	3.1	-22%
	t = 9 s	3.6	-9%	3.4	-15%	3.1	-22%
x = 120	t = 13 s	3.6	-9%	3.1	-22%	3.1	-22%
	t = 14 s	3.6	-9%	3.6	-9%	3.1	-22%
	t = 16 s	4.2	4%	3.6	-9%	3.1	-22%
	t = 19 s	4.2	4%	4.2	4%	2.9	-28%
	Average (abs)	3.7	9%	3.5	15%	3.1	22%
	Real width			6.0			
	t = 3 s	5.3	-12%	5.3	-12%	5.2	-13%
	t = 6 s	5.3	-12%	5.3	-12%	5.2	-13%
	t = 9 s	5.3	-12%	5.3	-12%	5.2	-13%
x = 130	t = 13 s	5.0	-16%	5.3	-12%	5.2	-13%
	t = 14 s	5.5	-8%	5.3	-12%	5.2	-13%
	t = 16 s	5.0	-16%	5.3	-12%	5.0	-17%
	t = 19 s	4.5	-25%	5.3	-12%	5.2	-13%
	Average (abs)	5.1	15%	5.3	12%	5.2	14%
	Real width			8.0			
	t = 3 s	6.2	-22%	7.0	-13%	6.7	-16%
	t = 6 s	6.0	-25%	7.0	-13%	6.7	-16%
	t = 9 s	6.5	-19%	7.0	-13%	6.7	-16%
x = 140	t = 13 s	6.5	-19%	7.0	-13%	6.7	-16%
	t = 14 s	6.2	-22%	7.0	-13%	6.7	-16%
	t = 16 s	6.0	-25%	6.7	-16%	6.7	-16%
	t = 19 s	6.0	-25%	6.7	-16%	7.0	-13%
	Average (abs)	6.2	23%	6.9	14%	6.8	16%
	Real width			10.0			
	t = 3 s	7.8	-23%	8.8	-13%	9.3	-8%
	t = 6 s	8.3	-18%	8.3	-18%	9.3	-8%
	t = 9 s	7.8	-23%	8.8	-13%	9.3	-8%
x = 150	t = 13 s	8.3	-18%	8.5	-15%	9.0	-10%
	t = 14 s	7.8	-23%	8.3	-18%	8.8	-13%
	t = 16 s	7.5	-25%	7.8	-23%	8.8	-13%
	t = 19 s	7.5	-25%	7.8	-23%	8.8	-13%
	Average (abs)	7.8	22%	8.3	17%	9.0	10%

* Width dimension in mm. Average is the absolute average.

At x = 110, the simulated average width measurements for defects 1A and 1B are 3.9 and 3.0 mm, respectively. These values overestimate the real width by more than 50%. By comparison, the simulated value of defect 1C is 2.2 mm or 10% greater than the real width.

Most defects' widths at x = 120 are smaller than the defects' real width, and all defects' average width accuracies are equal to or better than 22%.

All defects' widths at x = 130, x = 140, and x = 150 are smaller than the defects' real widths. Their average defect width accuracies are equal to or better than 15%, 23% and 22%, respectively, for all defects

Measurement consistency during the time reviewed is best at x = 130 and x = 140, followed by x = 150, x = 120, and x = 110. Generally, the simulated values better agree with the real defect width close to the heating termination at 13 s.

5.2 Experiment Results

The specimen's front surface temperature profiles are not smooth, and neither are their derivatives. For example, Fig. 7 shows the experiment temperature profiles and its derivative at x = 110. FWHM fails to estimate the defect width because the derivative cannot determine the local maximum and local minimum.

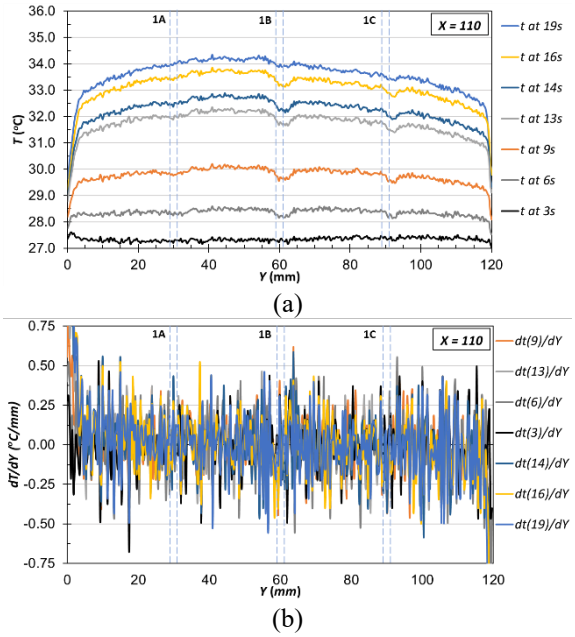

Fig. 7. (a) Experiment temperature profiles and (b) their first derivative at x = 110

The data-averaging method can reduce the local fluctuation in the temperature profiles. As a result, the temperature curve starts later in the averaged data. It is at y = 1.8 mm or the 6th data in the temperature profile. Fig. 8 shows the experiment temperature data-averaging profiles and their derivatives.

The defects are readily visible in the experiment's temperature profiles, except at x = 150 and t = 3 s. Additionally, it can be noticed that defects 1B and 1C are moving toward the specimen's upper side (curve's right side). The camera lens distortion causes these movements.

It becomes challenging to figure out the width of defect 1A at x = 110 and 120 because it is harder to identify the local extrema for defect 1A but not for defects 1B and 1C. All extrema for all defects can be identified at x = 130 and 140, allowing for the quick identification of all defects' widths.

At the edge of the specimen, x = 150, it is difficult to identify the local maximum and minimum of the defects since there are more local extrema present than are required to calculate the defects' width.

Table 5 shows the experimental results of the defects' width and their accuracy to the defects' real. The experimental averaged values overestimate the defect width for all defects at x = 110 by 90% or more, and it is large enough to be considered inaccurate for CFRP. Meanwhile, at x = 120, the average width for defect 1A is also not accurate enough, but as opposed to it, defects 1B and 1C have better accuracy. The difference is 40% or less. Almost all the defects' width measurements at x = 110 and 120 are bigger than their real width.

The defects' widths at x = 130 and 140 are mixed, larger, or smaller than their real widths. The average width generally agrees with the real width, with a difference of 21% or less. At x = 150, the average width accuracies seem to be good, which is better than 30% for all defects. However, as mentioned above, it loses significance due to difficulty picking the local maximum and minimum.

It is worth mentioning that the measurement results at t = 6s and t = 19s are not sufficiently consistent with the measurement at other times for all x positions. Therefore, the width data at these times cannot be used as a reference for the defect width.

To accurately and consistently determine the defects' width in the experiment, the derivative curves at x = 130 and x = 140, and t = 9, 13, 14 and 16 s are used. The average difference from the true width is less than 15% for 1A and 20% for 1B and 1C, respectively. As a comparison, the average difference is 23%, 14% and 16% for 1A, 1B, and 1C, respectively in the simulation for x = 130 and x = 140.

The experiment-measured defect widths are less accurate and somewhat less consistent than those obtained from the simulation. The further away from the center of the specimen, the lower the temperature in the x- and y-axis. The circular heat flux pattern in the experiment results in the highest heat intensity at the center of the specimen. The performance of the experimental measurements is lower than the simulation, mainly due to the above-mentioned non-uniform heating. The lens distortion also contributes to this lower performance by shifting specimen surface points, which increases the distance of the points toward the specimen edges.

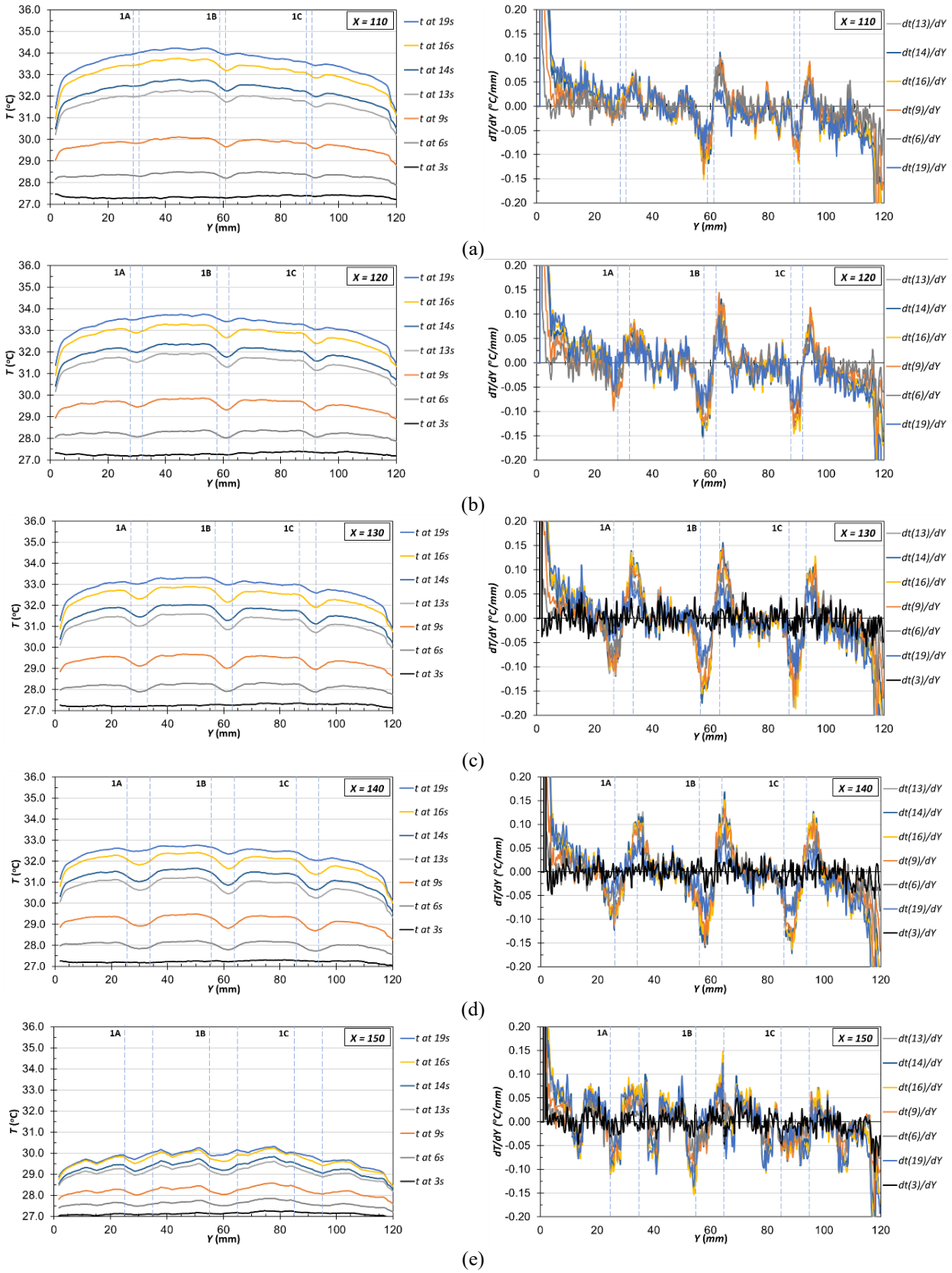

Fig. 8. Experiment temperature data-averaging profiles and their first derivative: (a) x = 110, (b) x = 120, (c) x = 130, (d) x = 140, and (e) x = 150

Table 5. Experiment defects' width

x-axis	Defects	1A		1B		1C	
		Width	Δ	Width	Δ	Width	Δ
x = 110	Real width			2.0			
	t = 6 s	-	-	5.3	167%	3.6	78%
	t = 9 s	8.2	309%	5.7	185%	3.9	96%
	t = 13 s	6.4	220%	5.7	185%	3.9	96%
	t = 14 s	6.8	238%	5.7	185%	3.9	96%
	t = 16 s	5.3	167%	5.3	167%	3.6	78%
	t = 19 s	-	-	5.7	185%	3.9	96%
	Average (abs)	6.7	234%	5.6	179%	3.8	90%
x = 120	Real width			4.0			
	t = 6 s	6.1	52%	6.4	61%	5.7	43%
	t = 9 s	7.2	79%	5.0	25%	5.7	43%
	t = 13 s	7.2	79%	5.7	43%	5.7	43%
	t = 14 s	7.2	79%	5.7	43%	5.7	43%
	t = 16 s	6.8	70%	4.3	7%	5.7	43%
	t = 19 s	-	-	6.4	61%	3.6	-10%
	Average (abs)	6.9	72%	5.4	40%	5.4	38%
x = 130	Real width			6.0			
	t = 6 s	6.5	8%	5.7	-4%	6.8	14%
	t = 9 s	5.4	-10%	7.2	20%	7.5	26%
	t = 13 s	5.4	-10%	7.2	20%	7.5	26%
	t = 14 s	5.4	-10%	7.2	20%	6.8	14%
	t = 16 s	5.4	-10%	7.2	20%	6.8	14%
	t = 19 s	-	-	6.5	8%	4.0	-34%
	Average (abs)	5.4	10%	7.0	15%	6.5	21%
x = 140	Real width			8.0			
	t = 6 s	10.1	26%	6.1	-23%	10.8	35%
	t = 9 s	8.3	4%	6.8	-14%	7.6	-5%
	t = 13 s	10.1	26%	6.8	-14%	7.2	-10%
	t = 14 s	9.4	17%	6.8	-14%	7.6	-5%
	t = 16 s	8.6	8%	6.8	-14%	7.6	-5%
	t = 19 s	10.1	26%	6.8	-14%	10.8	35%
	Average (abs)	9.3	18%	6.8	-17%	8.1	16%
x = 150	Real width			10.0			
	t = 6 s	12.3	23%	10.1	1%	14.1	41%
	t = 9 s	11.2	12%	10.1	1%	8.3	-17%
	t = 13 s	12.3	23%	10.1	1%	6.1	-39%
	t = 14 s	12.3	23%	10.1	1%	6.5	-35%
	t = 16 s	6.5	-35%	10.1	1%	6.1	-39%
	t = 19 s	12.3	23%	10.5	5%	9.4	-6%
	Average (abs)	10.9	23%	10.2	2%	7.3	29%

* Width dimension in mm. Average is the absolute average.

6. CONCLUSION

Based on this study's findings, it can be concluded that defect size/width can be detected by analyzing the temperature distribution over the model surface by simulation and experiment. The general summary is as follows:

- The temperature profile on the front surface can provide quantitative data about the embedded defects and indicate their positions.
- The FWHF method can estimate the defect's width by measuring the distance between the local maximum and local minimum of the derivative curve.
- The simulated values better agree with the real defect width close to the heating termination, 13s in this study, because the defects' temperature profiles are at their most prominent, and their derivatives values are at the highest extrema.
- The defect width is readily estimated for embedded defects larger than 6 mm based on the experimental temperature profiles processed by the data averaging and

FWHM. The estimated values are much larger than the true width for smaller defects.

The main findings based on the technique used to detect the defect are as the following.

- In the simulation, the shallower the defect, the higher the extrema peaks, and the easier the defect can be detected. The defect width estimated by FWHM is consistently 10% larger than the true width near the tip of defect 1C.
- The temperature profile is smooth in the simulation but not in the experiment. The averaging data technique is necessary for smoothing the experiment temperature profile before applying the FWHM method.
- The accuracy and consistency of the average defect width obtained by the simulation are higher than those obtained by the experiment.
- The camera lens distortion in this study made the specimen thermal image less accurate, leading to the experimental method's lower performance.
- As part of the future study, lens distortion will be corrected in order to improve the experimental results.

ACKNOWLEDGMENTS

This research is supported by the Ministry of Science and Technology, project number MOST 111-2221-E-324-008 and MOST 110-2221-E-324-006. The authors would like to thank Dr. Yung Chiang Lin for his valuable comments regarding experimental data processing.

REFERENCES

Avdelidis, N.P., Almond, D.P., Dobbinson, A., Hawtin, B.C., Ibarra-Castanedo, C., Maldague, X. 2004. Aircraft composites assessment by means of transient thermal NDT. Progress in Aerospace Sciences, 40, 143–162.

Chiang, C.H., Hidayat, M., Kumar, D. 2022. Simulated thermal image based on finite element models for a layered composite structures. Materials Today: Proceedings, 57, 871–877.

Karataş, M.A., Gökkaya, H. 2018. A review on machinability of carbon fiber reinforced polymer (CFRP) and glass fiber reinforced polymer (GFRP) composite materials. Defence Technology, 14, 318–326.

Marani, R., Campos-Delgado, D.U. 2023. Depth classification of defects in composite materials by long-pulsed thermography and blind linear unmixing. Composites Part B: Engineering, 248, 110359.

Meola, C., Boccardi, S., Carlomagno, G.M. 2016. Infrared thermography in the evaluation of aerospace composite materials: Infrared thermography to composites. Woodhead Publishing. Cambridge. UK.

Poelman, G., Hedayatrasa, S., Segers, J., Paepegem, W.V., Kersemans, M. 2020. Adaptive spectral band integration in flash thermography: Enhanced defect detectability and quantification in composites. Composites Part B: Engineering, 202, 108305.

Quintanas-Corominas, A., Reinoso, J., Casoni, E., Turon, A., Mayugo, J.A. 2019. A phase field approach to simulate intralaminar and translaminar fracture in long fiber composite materials. Composite Structures, 220, 899–911.

Sirikham, A., Zhao, Y., Liu, H., Xu, Y., Williams, S., Mehnen, J. 2020. Three-dimensional subsurface defect shape reconstruction and visualisation by pulsed thermography. Infrared Physics & Technology, 104, 103151.

Vavilov, V.P. 2022. 3D modeling of pulsed thermal NDT: Back to basic features and subtle phenomena. NDT & E International, 130, 102659.

Vavilov, V., Burleigh, D. 2020. Infrared thermography and thermal nondestructive testing. Springer Nature. Switzerland AG.

Xu, C., Zhang, W., Wu, C., Xie, J., Yin, X., Chen, G. 2020. An improved method of eddy current pulsed thermography to detect subsurface defects in glass fiber reinforced polymer composites. Composite Structures, 242, 112145.

Wang, Z., Wan, L., Zhu, J., Ciampa, F. 2022. Evaluation of defect depth in CFRP composites by long pulse thermography. NDT & E International, 129, 102658.

Zalameda, J., Winfree, W. 2018. Detection and characterization of damage in quasi-static loaded composite structures using passive thermography. Sensors, 18, 3562.

Zhuo, L., Yang, X., Zhu, J., Huang, Z., Chao, J., Xie, W. 2023. Size determination of interior defects by reconstruction of subsurface virtual heat flux for step heating thermography. NDT & E International, 133, 102734.